ACS APPLIED MATERIALS & INTERFACES

www.acsami.org

Research Article

Dual-Signaling Electrochemical Ratiometric Method for Competitive Immunoassay of CYFRA21-1 Based on Urchin-like Fe_3O_4@PDA-Ag and $Ni_3Si_2O_5(OH)_4$-Au Absorbed Methylene Blue Nanotubes

Liu Qu, Lei Yang, Yueyuan Li, Xiang Ren, Huan Wang, Dawei Fan, Xueying Wang,* Qin Wei,* and Huangxian Ju*

Cite This: *ACS Appl. Mater. Interfaces* 2021, 13, 5795−5802

Read Online

ACCESS | Metrics & More | Article Recommendations | Supporting Information

ABSTRACT: A novel ratiometric electrochemical (EC) sensing platform was established for sensitive immunoassay of target cytokeratin 19 fragment 21-1 (CYFRA21-1) biomarker by combining competitive immunoreaction and multisignal output. This immunosensor utilized Ag nanoparticles (NPs)-functionalized urchin-like Fe_3O_4@polydopamine (u-Fe_3O_4@PDA-Ag) as a matrix to immobilize CYFRA21-1 antigens and methylene blue (MB)-absorbed $Ni_3Si_2O_5(OH)_4$-Au nanotubes (NTs) to label the anti-CYFRA21-1 (Ab). During the competitive immunoreaction, square wave voltammetric (SWV) current changes of Ag NPs from u-Fe_3O_4@PDA-Ag indicator and MB from $Ni_3Si_2O_5(OH)_4$-Au/MB indicator are relevant to the dosage of CYFRA21-1-acquired $Ni_3Si_2O_5(OH)_4$-Au/MB/Ab. More importantly, numerous CYFRA21-1 loaded stably on u-Fe_3O_4@PDA-Ag exhibited strong competitive capacity toward the target-CYFRA21-1 to combine $Ni_3Si_2O_5(OH)_4$-Au/MB/Ab, causing sensitive changes in the ratio of two measured SWV currents. Prominently, "$\Delta I = \Delta I_{MB} + |\Delta I_{Ag\ NPs}|$" ($\Delta I_{MB}$ and $|\Delta I_{Ag\ NPs}|$ represents the change values of the oxidation peak currents of MB and Ag NPs, respectively) could be regarded as significantly amplifying the signal response and ultimately improving the sensitivity of CYFRA21-1 detection, from which we derived a wide dynamic range from 500 fg/mL to 50 ng/mL and a low detection limit of 0.39 pg/mL (S/N = 3). This work may exert a profound impact on monitoring other biomarkers in early diagnosis of diseases.

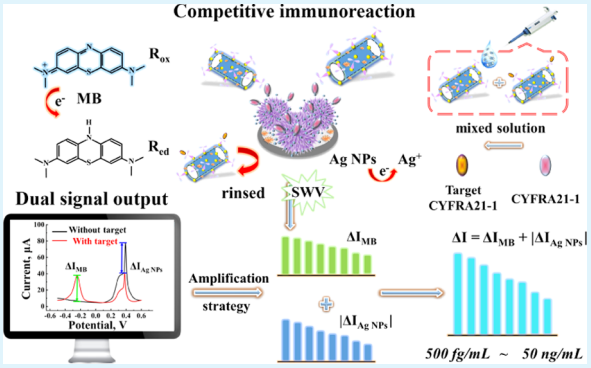

KEYWORDS: *multisignal output, competitive immunoreaction, ratiometric, Ag-functionalized urchin-like Fe_3O_4@PDA, MB-absorbed $Ni_3Si_2O_5(OH)_4$-Au NTs*

INTRODUCTION

Currently, nonsmall cell lung cancer (NSCLC) has been regarded as one of the leading factors to cause global cancer death.[1] It is of great significance to assess the level of tumor markers in the field of diagnosis, prognosis, staging, and monitoring the growth of the tumor.[2] Notably, cytokeratin 19 fragment 21-1 (CYFRA21-1) as the biomarker of NSCLC exhibits critical significance for assessing early therapeutic response and predicting the survival rate of NSCLC.[3,4] Biosensor has obtained substantial attention in analyzing tumor targets.[5−7] Considering the merits of high sensitivity, wide dynamic range, low cost, miniaturization, and fast response time, electrochemical (EC) immunoassay has been extensively employed for the detection of tumor markers.[8−10] Strikingly, compared with different single-signal amplification strategies that only involve "signal-on" or "signal-off" mode, the ratiometric EC immunosensor involves dual signal output and effectively eliminates the environmental impact and background noise, which could significantly improve the accuracy and sensitivity in the detection of CYFRA21-1.[11,12] Importantly, the ratio of two signal output in a ratiometric immunosensor is regarded as the basis for quantitative biomarker analysis.[13,14] Consequently, application of the sensing substrate (one signal indicator) and the label material (another signal indicator) is undoubtedly one of the keys to ensure the high sensitivity of the ratiometric EC immunosensor.

Nowadays, it is worth mentioning that silver nanoparticles (Ag NPs) together with their derivatives as the electron-transfer mediator are foreseen as promising candidates for extensive application in biosensing fields. That is because of

Received: November 11, 2020
Accepted: January 13, 2021
Published: January 22, 2021

https://dx.doi.org/10.1021/acsami.0c20049
ACS Appl. Mater. Interfaces 2021, 13, 5795−5802

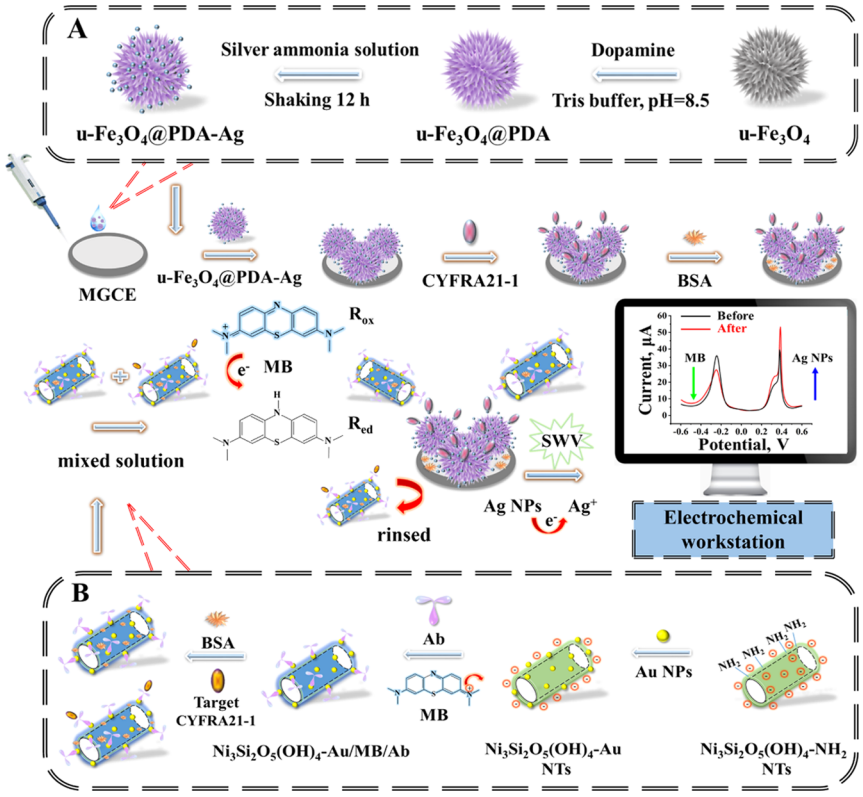

Figure 1. Illustration of the ratiometric EC sensing platform design: (A) preparation of u-Fe_3O_4@PDA-Ag; (B) preparation of the mixture solution of $Ni_3Si_2O_5(OH)_4$-Au/MB/Ab labels and varying concentrations of target-CYFRA21-1.

their unique merits including extraordinary biocompatibility, appealing catalytic activity, and brilliant conductivity.[15−17] Furthermore, polymer materials with semiconductor properties have also exerted prominent effects in biosensing applications owing to features with abundant function groups that can exhibit efficient interactions with target molecules or ions.[18−20] Notably, polydopamine (PDA) with ample catechol and amine groups could significantly promote the reduction of Ag^+ to Ag NPs on its surface. Simultaneously, the deposited Ag NPs are uniform in size and exhibit high stability and low van der Waals forces so as to effectively prevent themselves from agglomeration.[21−23] Instead of smooth spherical Fe_3O_4, the selected carrier magnetic urchin-like Fe_3O_4 (u-Fe_3O_4) with higher specific surface area was covered with more of PDA thin shell to provide abundant Ag NP-functionalized active sites.[24] In addition, the magnetic glass carbon electrode (MGCE) was employed to firmly immobilize the matrix. In combination with the above-mentioned features, the application of the obtained core−shell u-Fe_3O_4@PDA-Ag of this paper presents several advantages. (1) u-Fe_3O_4@PDA-Ag acting as a signal indicator could provide a strong signal output in view of its excellent EC performance and (2) unique magnetic properties that allow u-Fe_3O_4@PDA-Ag to be firmly fixed on the MGCE surface. Therefore, applying u-Fe_3O_4@PDA-Ag in constructing the sensing platform could greatly improve its sensitivity and stability.

Recently, silicate nanomaterials, especially silicate nanotubes (NTs), have been reported as promising candidates for various applications (including catalysis, controlled release of pharmaceuticals, and separation).[25,26] Notably, the significant dye-binding capacity makes nickel silicate ($Ni_3Si_2O_5(OH)_4$) NTs a promising nanoadsorbent.[27,28] Taking advantage of the firm electrostatic interaction, the cationic dye methylene blue (MB) as an electron-transfer mediator could be absorbed on anionic $Ni_3Si_2O_5(OH)_4$ NTs to provide a signal output directly. Additionally, $Ni_3Si_2O_5(OH)_4$ NTs possess absolute adsorption capacity toward MB, which is profited from numerous negative charge provided by the abundant hydroxyl groups and silanol groups on the surface of its unique multiwalled hollow architecture.[29] Furthermore, the aminated $Ni_3Si_2O_5(OH)_4$ NTs could be linked to Au NPs through Au-NH_2 bound to improve electron-transfer efficiency and realized remarkable enhancement of the EC signal. Meanwhile, the obtained $Ni_3Si_2O_5(OH)_4$-Au NTs could ensure the successful linkage of antibody (Ab) and thus further prevent the leakage of MB. Consequently, an outstanding EC signal of MB could also be pursued from the $Ni_3Si_2O_5(OH)_4$-Au/MB signal indicator.

Excellent dual EC signal output offered a favorable foundation for realizing obvious changes in the ratio of two signals. Moreover, competitive immunoreaction was also employed as a key to effectively improve the sensitivity. Typically, the competitive sensing mechanism depends on the competition between labeled and unlabeled biomolecules for the number of finite binding sites based on immune responses.[30] Different from the sandwich model, it only involves one Ab, the fabrication principle is more suitable for small-molecule CYFRA21-1 detection. In detail, utilizing abundant CYFRA21-1, which were immobilized on the u-Fe_3O_4@PDA-Ag matrix and target-CYFRA21-1 competed efficiently to acquire the $Ni_3Si_2O_5(OH)_4$-Au/MB/Ab. Hence, sensitive variation in the dosage of $Ni_3Si_2O_5(OH)_4$-Au/MB/Ab acquired by CYFRA21-1 was achieved and from which further obvious changes of the ratio was derived. In view of the above, a novel ratiometric EC immunosensor was proposed in

https://dx.doi.org/10.1021/acsami.0c20049
ACS Appl. Mater. Interfaces 2021, 13, 5795−5802

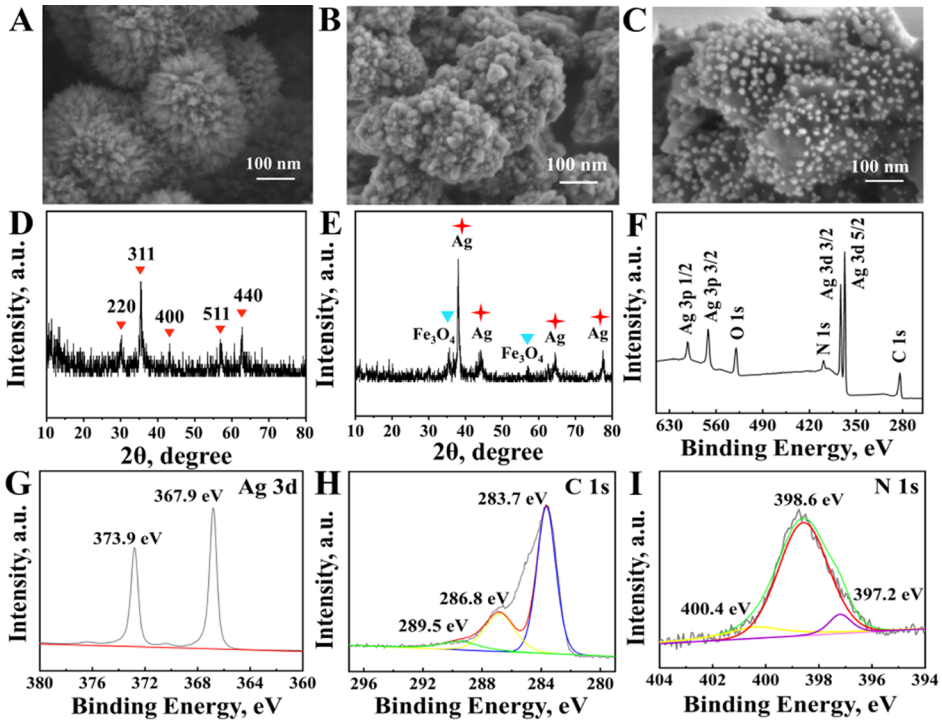

Figure 2. SEM images of the u-Fe_3O_4 (A), u-Fe_3O_4@PDA (B), and u-Fe_3O_4@PDA-Ag microspheres (C). XRD patterns of the u-Fe_3O_4 (D) and u-Fe_3O_4@PDA-Ag microspheres (E). Survey scan XPS spectrum (F), high-resolution XPS spectra of (G) Ag 3d, (H) C 1s, and (I) N 1s regions for the u-Fe_3O_4@PDA-Ag microspheres.

this work to achieve high-sensitivity detection of CYFRA21-1. Notably, compared with the single "$|\Delta I_{Ag\ NPs}|$" or "ΔI_{MB}", a distinct signal amplification strategy utilized "$\Delta I = \Delta I_{MB} + |\Delta I_{Ag\ NPs}|$" as the response signal provided a lower limit of detection (LOD) and absolutely sensitive signal variation. The combination of competitive immunoreaction together with the multisignal output of the ratiometric EC sensing platform should provide a novel avenue and versatile approach for future sensitive monitoring of CYFRA21-1.

EXPERIMENTAL SECTION

Preparation of $Ni_3Si_2O_5(OH)_4$-Au/MB/Ab Labels. The synthesis steps of Au NPs, $Ni_3Si_2O_5(OH)_4$ NTs, and $Ni_3Si_2O_5(OH)_4$-NH_2 NTs are listed in the Supporting Information. One hundred milligrams of $Ni_3Si_2O_5(OH)_4$-NH_2 NTs was dispersed in 400 mL of Au NPs under continuous shaking for 12 h; then, $Ni_3Si_2O_5(OH)_4$-Au was washed thoroughly and dried in a vacuum. Subsequently, 1 mL of Ab solution (10 μg/mL) was mixed with 1 mL of the prepared $Ni_3Si_2O_5(OH)_4$-Au solution (2.0 mg/mL), and the mixture was incubated at 4 °C overnight. The obtained $Ni_3Si_2O_5(OH)_4$-Au/Ab was centrifuged and redispersed in 1 mL of PBS solution. Afterward, 0.8 mL of MB solution (10 mg/mL) was added to the above $Ni_3Si_2O_5(OH)_4$-Au/Ab solution and incubated at 4 °C for 12 h. Finally, the resulting $Ni_3Si_2O_5(OH)_4$-Au/MB/Ab was centrifuged, redispersed in 1 mL of PBS solution, and stored at 4 °C for further use.

Fabrication Process of the Ratiometric Immunosensor. Figure 1 illustrates the fabrication process of the proposed ratiometric EC sensing platform based on competitive immunoreaction. Initially, MGCE (4 mm in diameter) was polished using different alumina slurries (1.0, 0.3, and 0.05 μm) to obtain a mirrorlike surface, washed thoroughly with water, and dried with flowing nitrogen. Afterward, 6 μL of the dispersed u-Fe_3O_4@PDA-Ag solution (1.2 mg/mL) was modified onto the well-polished surface of MGCE and dried naturally. Next, the electrode was assembled using 6 μL of CYFRA21-1 (1 μg/mL) for 1 h of incubation at 4 °C. After rinsing, the excess CYFRA21-1 was removed. Then, bovine serum albumin (BSA) was used to block the nonspecific binding sites of $Ni_3Si_2O_5(OH)_4$-Au/MB/Ab. Varying concentrations of target-CYFRA21-1 was mixed with $Ni_3Si_2O_5(OH)_4$-Au/MB/Ab in a 1:1 volume ratio, and the mixture was incubated under 4 °C overnight for further use. Meanwhile, 3 μL of BSA (0.1 wt %) was also coated onto the electrode surface for 1 h to block nonspecific binding sites. Then, the excess BSA was washed thoroughly with PBS. Following that, 6 μL of the prepared mixture solution (target-CYFRA21-1 and $Ni_3Si_2O_5(OH)_4$-Au/MB/Ab) was modified and incubated for another 1 h, from which CYFRA21-1 competed against target-CYFRA21-1 to acquire $Ni_3Si_2O_5(OH)_4$-Au/MB/Ab. Eventually, the modified MGCE was thoroughly rinsed with PBS and the proposed EC sensing platform was ready to be used for EC measurement tests.

EC Measurements. EC measurement performed on the final fabricated electrode mainly included the square wave voltammetry (SWV) method. Under the three-electrode system, SWV was recorded (range and direction: from −0.6 to 0.6 V, increase: 0.004 V, amplitude: 0.025 V, frequency: 15 Hz) at room temperature in 10 mL of PBS (pH 7.0). The detected SWV signal of the immunosensor was related to the concentration of target-CYFRA21-1.

ANALYSIS OF RESULTS

Characterization of the Prepared Nanomaterials. In Figure 2A–C, the scanning electron microscopy (SEM) images were employed to characterize the morphology of the u-Fe_3O_4, u-Fe_3O_4@PDA together with u-Fe_3O_4@PDA-Ag microspheres. As shown in Figure 2A, the Fe_3O_4, which owns a mean diameter of 350 nm, assembled from numerous ultrathin nanoflakes and exhibited the urchin-like morphology. Figure 2B presents the PDA thin layer wrapped on the surface of u-Fe_3O_4 to form u-Fe_3O_4@PDA particles.[31] After in situ growth, Ag NPs can be clearly observed loading onto the PDA shell surface (Figure 2C). Meanwhile, morphologies of the above three materials were further demonstrated by transmission electron microscopy (TEM) in Figure S3A–C

https://dx.doi.org/10.1021/acsami.0c20049
ACS Appl. Mater. Interfaces 2021, 13, 5795−5802

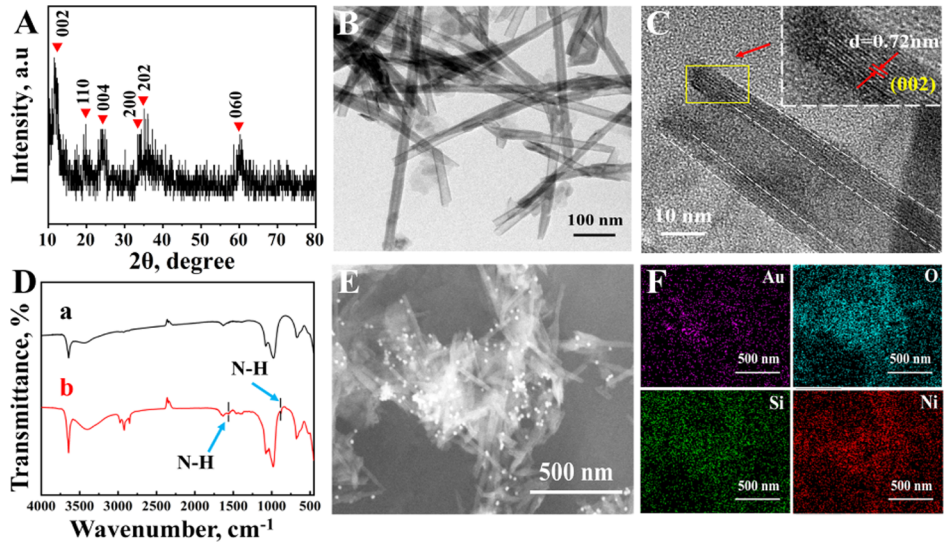

Figure 3. XRD pattern of $Ni_3Si_2O_5(OH)_4$ NTs (A). TEM (B) and HRTEM (C) of $Ni_3Si_2O_5(OH)_4$ NTs. FTIR spectrum (D) of $Ni_3Si_2O_5(OH)_4$ NTs (curve a) and $Ni_3Si_2O_5(OH)_4$-NH_2 NTs (curve b). SEM image (E) and EDS element mappings (F) of $Ni_3Si_2O_5(OH)_4$-Au NTs.

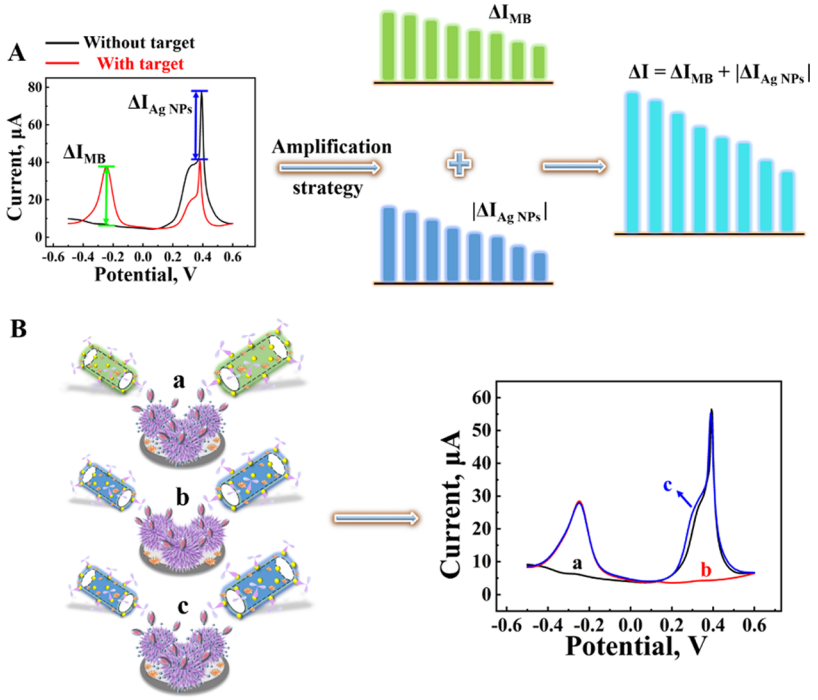

Figure 4. (A) Signal amplification strategy of the dual-signaling EC ratiometric immunosensor based on the competitive construction mode. (B) SWV response of three modified immunosensors: only in the presence of Ag NPs (curve a); only in the presence of MB (curve b); and in the presence of both Ag NPs and MB (curve c).

(Supporting Information). As shown in Figure 2D, the X-ray diffraction (XRD) pattern was displayed to characterize the u-Fe_3O_4 crystallization, from which all of the diffraction peaks were found to match well with the spinel cubic phase Fe_3O_4 (JCPDS Card No. 65-3107). Figure 2E illustrates the XRD spectrum of the obtained u-Fe_3O_4@PDA-Ag, in which the strong additional diffraction peaks of Ag NPs could be clearly observed (in addition to the existing diffraction peaks of Fe_3O_4). Furthermore, energy-dispersive spectrometer (EDS) spectrum (Figure S1A) as well as the EDS element mappings (Figure S1B) further confirmed the existence of Fe, O, N, C, and Ag elements. The Brunauer−Emmett−Teller (BET) method (Figure S2) described in the Supporting Information was utilized to validate the superior specific surface area of u-Fe_3O_4 in contrast with spherical-like structure. In addition, X-ray photoelectron spectroscopy (XPS) survey spectrum of u-Fe_3O_4@PDA-Ag (Figure 2F−I) also convincingly proved the presence of Ag, O, N, and C elements in this particle, the details are shown in the Supporting Information. The above characterization results proved the successful synthesis of the u-Fe_3O_4@PDA-Ag microspheres.

Additionally, the XRD pattern (Figure 3A) was also applied to characterize the crystallinity of $Ni_3Si_2O_5(OH)_4$ NTs. The characteristic diffraction peaks were all indexed to correspond

https://dx.doi.org/10.1021/acsami.0c20049
ACS Appl. Mater. Interfaces 2021, 13, 5795−5802

to the (002), (110), (004), (200), (202), and (060) planes of $Ni_3Si_2O_5(OH)_4$ NTs, respectively (JCPDS Card No. 49-1859). As illustrated in the TEM image (Figure 3B), the $Ni_3Si_2O_5(OH)_4$ NTs exhibited an outer diameter of about 20 nm and a length of several hundred nanometers. Moreover, the multiwalled hollow tubular structure and the existence of the representative lattice was proved by HRTEM (Figure 3C). Furthermore, the FTIR spectrum (Figure 3D) described in the Supporting Information was used for recording the NH_2 functional group of $Ni_3Si_2O_5(OH)_4$-NH_2 NTs. To prove the successful synthesis of $Ni_3Si_2O_5(OH)_4$-Au NTs, the SEM image (Figure 3E) and its corresponding mapping (Figure 3F) were utilized to characterize the morphology and demonstrate the existence of Si, O, Ni, and Au elements simultaneously. Besides, the ultraviolet−visible (UV−vis) spectroscopy (Figure 5A) clearly validated that $Ni_3Si_2O_5(OH)_4$-Au/MB was obtained. Compared with pure $Ni_3Si_2O_5(OH)_4$ NTs (curve a) without any absorption peak, $Ni_3Si_2O_5(OH)_4$-Au NTs (curve b) exhibited an absorption peak at around 520 nm.[32] Furthermore, the additional peak at about 660 nm (curve c) indicated the successful adsorption of MB on $Ni_3Si_2O_5(OH)_4$-Au NTs.[22] Meanwhile, the ζ-potential presented in the Supporting Information provided another intuitive proof information for the above opinion.

Mechanism of Signal Amplification Strategy and Feasibility of the EC Immunosensor. In this work, the signal amplification strategy of the proposed novel ratiometric EC immunosensor is shown in Figure 4A. Herein, $\Delta I = \Delta I_{MB} + |\Delta I_{Ag\ NPs}|$ was defined as the response signal to amplify the EC response. Also, in this amplification strategy compared with the ΔI_{MB} or $|\Delta I_{Ag\ NPs}|$, the proposed "ΔI" exhibited the more sensitive signal variation that achieved an obvious signal amplification.

To investigate the feasibility of the proposed EC immunosensor, herein, SWV curve response was employed to evaluate three different modified electrodes. The corresponding results are shown in Figure 4B. In $Ni_3Si_2O_5(OH)_4$-Au/Ab as the label in the absence of MB (a), only an oxidation peak current of Ag NPs could be observed at around 0.38 V. Similarly, u-Fe_3O_4@PDA as the matrix in the absence of Ag NPs (b) only has an oxidation peak current of MB at about −0.25 V. However, in the presence of Ag NPs and MB (c), both their oxidation peak currents appeared and did not interfere with each other. According to the competitive construction adopted in this work, the above results indicated that Ag NPs (u-Fe_3O_4@PDA-Ag) act as signal-on type, whereas MB ($Ni_3Si_2O_5(OH)_4$-Au/MB/Ab) acts as a signal-off type. Hence, the feasibility of the proposed ratiometric EC method combined with signal-on and signal-off strategies for competitive immunoassay of CYFRA21-1 was completely acceptable.

EC Characterization and EC Impedance Spectroscopy (EIS) Characterization of the Immunosensor. As illustrated in Figure 5B, cyclic voltammetry (CV) conducted in a 5 mmol/L $K_3[Fe(CN)_6]$ solution was utilized to verify the superior EC performance of the u-Fe_3O_4@PDA-Ag substrate. The specific contrast experiments are presented in the Supporting Information.

In this work, the SWV curve response and electrochemical impedance spectroscopy (EIS) were applied to investigate the step-by-step assembly process of the fabricated EC immunosensor.[33] In Figure 5C, apparently, there was no SWV response for bare MGCE (curve a). Next, modification of u-Fe_3O_4@PDA-Ag increased the SWV response to about 76 μA (curve b). With the following modification of CYFRA21-1 (curve c) and BSA (curve d) in turn, the SWV response decreased layer by layer due to the steric hindrance effect of nonconductive biomolecules that blocked the electron transfer. Subsequently, after the modification with $Ni_3Si_2O_5(OH)_4$-Au/MB/Ab, MB SWV response was introduced. Meanwhile, the SWV response of Ag NPs decreased significantly, which is mainly because the specific immunoreaction recognition occurring between CYFRA21-1 antibodies and antigens hindered electron transfer. The above results indicated the successful fabrication of the proposed immunosensor.

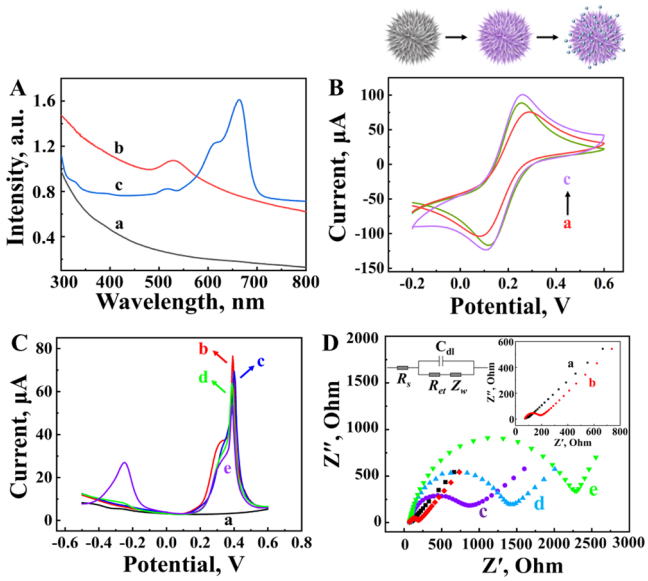

Figure 5. (A) UV−vis image of $Ni_3Si_2O_5(OH)_4$ (a), $Ni_3Si_2O_5(OH)_4$-Au (b), and $Ni_3Si_2O_5(OH)_4$-Au/MB (c). (B) CV responses of the immunosensor for different materials in 5 mmol/L $K_3[Fe(CN)_6]$: (a) u-Fe_3O_4, (b) u-Fe_3O_4@PDA, and (c) u-Fe_3O_4@PDA-Ag. (C) SWV response range from −0.6 to 0.6 V in PBS (10 mL, pH = 7.0). (D) EIS spectra of different modified electrodes in $Fe(CN)_6^{3-/4-}$ containing 0.1 mmol/L KCl solution, (a) MGCE, (b) MGCE/u-Fe_3O_4@PDA-Ag, (c) MGCE/u-Fe_3O_4@PDA-Ag/CYFRA21-1, (d) MGCE/u-Fe_3O_4@PDA-Ag/CYFRA21-1/BSA, and (e) MGCE/u-Fe_3O_4@PDA-Ag/CYFRA21-1/BSA/$Ni_3Si_2O_5(OH)_4$-Au/MB/Ab.

Nyquist plots of EIS results (Figure 5D) recorded in 2.5 mM $[Fe(CN)_6]^{3-/4-}$ PBS solution containing 0.1 M KCl were in accordance with those from the above SWV results. In Figure 5D, it is obvious that bare MGCE (curve a) exhibited an almost straight plot, which represented the comparatively small charge-transfer resistance. However, the semicircle at u-Fe_3O_4@PDA-Ag (curve b) got a little increase but not apparent, implying that it had good conductive property and electron-transfer capacity. After the modification of CYFRA21-1 (curve c) and BSA (curve d) layer by layer, the semicircle domain increased gradually. Similarly, it revealed the resistance of nonconductive biomolecules to electron transfer during the assembly process. Furthermore, the semicircle at $Ni_3Si_2O_5(OH)_4$-Au/MB/Ab (curve e) got a sharp increase due to the significant hindrance to electron transfer in the process of biomolecular specific recognition. The above EIS results further proved that the immunosensor has been fabricated successfully.

Herein, SWV was also employed to verify that u-Fe_3O_4@PDA-Ag (1.2 mg/mL) modified on the MGCE guaranteed a

https://dx.doi.org/10.1021/acsami.0c20049
ACS Appl. Mater. Interfaces 2021, 13, 5795−5802

more stable signal response readout than that generated by the GCE. As exhibited in Figure S6 (Supporting Information), from samples 1 to 5 (which represents 0, 1, 2, 3, and 5 min, respectively), it is clear that the current response for GCE exhibited a dramatic decline while the current response for MGCE exhibited satisfactory stability with the increase of time. The above results indicated that it is the magnetic interaction between u-Fe_3O_4@PDA-Ag and MGCE greatly contributed to the improvement of the stability of the proposed immunosensor.

Optimization of the Sensing System. The pH environment is a key factor that significantly influences the activity of bioprotein, thus affecting the EC performance. It is of great importance to optimize the pH value. As shown in Figure S5A, the EC behaviors of u-Fe_3O_4@PDA-Ag and $Ni_3Si_2O_5(OH)_4$-Au/MB/Ab were explored through SWV with pH ranging from 5.3 to 8.0. It is obvious that the optimal SWV responses were all obtained at pH 7.0. The concentrations of u-Fe_3O_4@PDA-Ag and $Ni_3Si_2O_5(OH)_4$-Au/MB/Ab could directly affect the sensitivity of the sensing system because both of the Ag NPs and MB acted as the signal markers to ensure the signal readout. From Figure S5B,C, it is clear that 1.2 mg/mL of u-Fe_3O_4@PDA-Ag and 1.6 mg/mL of $Ni_3Si_2O_5(OH)_4$-Au/MB/Ab were selected as the optimal concentration, respectively. It is worth noting that the amount of CYFRA21-1 immobilized on the u-Fe_3O_4@PDA-Ag substrate is also very important for the sensitivity of the immunosensor. Eventually, as shown in Figure S5D, 6 μL of 1 μg/mL of CYFRA21-1 was chosen and the specific conditional optimization process is described in the Supporting Information. According to the above results under optimal experiment conditions, the proposed novel ratiometric EC immune sensing platform could exhibit great performance for sensitive detection of CYFRA21-1.

Analytical Performance. Under the above optimal experimental conditions, the ratiometric EC immunosensor was employed to achieve a competitive immunoassay of CYFRA21-1 with diverse concentrations. Figure 6A exhibits descending trend of the SWV oxidation peak current of MB and ascending trend of the SWV oxidation peak current of Ag NPs with concentrations of CYFRA21-1 varying from 500 fg/mL to 50 ng/mL. As shown in Figure 6B, the linear relationship for this concentration range was represented by the equation ΔI_{MB} (μA) = $-3.28 \log c$ (ng/mL) + 21.25 (R^2 = 0.9912) and $\Delta I_{Ag\ NPs}$ (μA) = $4.23 \log c$ (ng/mL) − 20.22 (R^2 = 0.9969). With reference to the MB signal and the Ag NPs signal, the limit of detection (LOD) was calculated to 0.47 and 0.48 pg/mL (S/N = 3), respectively. As illustrated in Figure 6C, "$\Delta I_{MB}/|\Delta I_{Ag\ NPs}|$" response signal value also presented linear relationship for this concentration range with the linear regression equation of $\Delta I_{MB}/|\Delta I_{Ag\ NPs}| = 0.045 \log c$ (ng/mL) + 1.061 (R^2 = 0.9729). Figure 6D clearly shows that the amplified response signal value of $\Delta I = \Delta I_{MB} + |\Delta I_{Ag\ NPs}|$ decreased linearly in the range of 500 fg/mL to 50 ng/mL. The linear regression equation is $\Delta I = -7.51 \log c$ (ng/mL) + 41.24 (R^2 = 0.9953) and the LOD was as low as 0.39 pg/mL (S/N = 3), which indicated the defined ΔI obviously realized the signal amplification and achieved lower LOD compared with the ΔI_{MB} or "$\Delta I_{Ag\ NPs}$" as the single response signal. Furthermore, as shown in Table S2, compared with those previously reported detection methods for CYFRA21-1, the proposed immunosensor exhibited lower LOD, which demonstrated its prospect in practical applications for sensitive detection of CYFRA21-1.

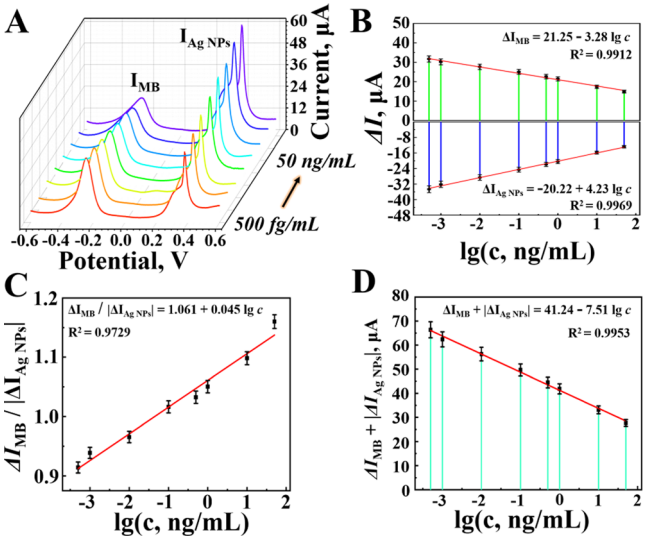

Figure 6. (A) SWV current responses of the EC immunosensor for CYFRA21-1 detection in the presence of 0.0005, 0.001, 0.01, 0.1, 0.5, 1, 10, and 50 ng/mL CYFRA21-1; calibration curves correlating the logarithm of ΔI_{MB} and $\Delta I_{Ag\ NPs}$ (B), $\Delta I_{MB}/|\Delta I_{Ag\ NPs}|$ (C), and $\Delta I = \Delta I_{MB} + |\Delta I_{Ag\ NPs}|$ (D) with the variation of the logarithm of CYFRA21-1 concentrations (from 500 fg/mL to 50 ng/mL). Error bars = RSD (n = 5).

Real Sample Analysis. For the assessment of the applicability of the proposed ratiometric EC immunosensor in practical samples, CYFRA21-1 in the healthy human blood serum samples was quantitatively detected by this immunosensor. The healthy human blood was pretreated to obtain the human serum samples with the following dilution with a PBS buffer solution (pH 7.4) to a level within the calibration range. Subsequently, the standard addition method was employed to implement the recovery experiments. From the results listed in Table 1, it is noted that in the tested samples, the RSD of CYFRA21-1 was 2.7−4.3% and the recovery range was 98.1−101.7% (n = 5), revealing satisfactory recoveries and potential practical applications in the CYFRA21-1 assay.

CONCLUSIONS

To summarize, a novel ratiometric EC immunosensor was successfully constructed by combing the competitive immunoreaction and multisignal out. In this strategy, the strong dual signal output, which was generated by the sensing the substrate u-Fe_3O_4@PDA-Ag (one signal indicator) as well as the label $Ni_3Si_2O_5(OH)_4$-Au/MB (another signal indicator) could provide a favorable foundation for obvious variation of the ratio. In addition, a large quantity of CYFRA21-1, which is loaded stably on the modified u-Fe_3O_4@PDA-Ag, could compete efficiently with target-CYFRA21-1 for immune recognition of $Ni_3Si_2O_5(OH)_4$-Au/MB labeled Ab. Hence, further obvious changes of the ratio were derived owing to the utilization of the competitive immunoreaction. Notably, the sensing strategy features admirable sensitivity as well as the remarkable signal amplification, which could originate from $\Delta I = \Delta I_{MB} + |\Delta I_{Ag\ NPs}|$ as the response signal for CYFRA21-1 detection. It turned out that the linear range is 500 fg/mL−50 ng/mL with a LOD of 0.39 pg/mL (S/N = 3). In view of the above statements, the EC immunosensor exhibits satisfied selectivity, acceptable reproducibility, and superb stability,

https://dx.doi.org/10.1021/acsami.0c20049
ACS Appl. Mater. Interfaces 2021, 13, 5795−5802

Table 1. Spike Recovery Test of CYFRA21-1 in Human Serum Samples

found CYFRA21-1 in diluted serum (pg/mL)	average (pg/mL)	addition content (pg/mL)	detection content (pg/mL)	average (pg/mL)	RSD (%, n=5)	recovery (%)
25.04, 23.12, 24.48, 22.02, 21.28		5.00	27.28, 28.24, 29.18, 27.42, 29.24	28.27	3.3	101.7
		10.00	34.25, 32.51, 31.97, 35.18, 32.21	33.22	4.3	100.4
	23.19	20.00	45.05, 43.02, 44.56, 41.69, 40.86	43.04	4.2	99.2
		50.00	74.58, 73.41, 71.44, 70.27, 75.25	72.99	2.9	99.6
		100.00	125.65, 121.10, 123.41, 118.68, 117.77	121.32	2.7	98.1

providing the sensing platform broad potential applicability in the sensitive detection of other biomarkers in clinical diagnosis.

■ ASSOCIATED CONTENT

Supporting Information

The Supporting Information is available free of charge at https://pubs.acs.org/doi/10.1021/acsami.0c20049.

Detailed reagents and apparatus, synthetic procedures of additional nanomaterials, TEM, FTIR, XPS spectra data, and additional nanomaterials characterization, additional EC experimental details, and analysis of the immunosensor performance can be found in the supporting information (PDF)

■ AUTHOR INFORMATION

Corresponding Authors

Xueying Wang − *Collaborative Innovation Center for Green Chemical Manufacturing and Accurate Detection, Key Laboratory of Interfacial Reaction & Sensing Analysis in Universities of Shandong, School of Chemistry and Chemical Engineering, University of Jinan, Jinan 250022, Shandong, China*; Email: ch_wangxy@ujn.edu.cn

Qin Wei − *Collaborative Innovation Center for Green Chemical Manufacturing and Accurate Detection, Key Laboratory of Interfacial Reaction & Sensing Analysis in Universities of Shandong, School of Chemistry and Chemical Engineering, University of Jinan, Jinan 250022, Shandong, China*; orcid.org/0000-0002-3034-8046; Email: sdjndxwq@163.com

Huangxian Ju − *Collaborative Innovation Center for Green Chemical Manufacturing and Accurate Detection, Key Laboratory of Interfacial Reaction & Sensing Analysis in Universities of Shandong, School of Chemistry and Chemical Engineering, University of Jinan, Jinan 250022, Shandong, China*; orcid.org/0000-0002-6741-5302; Email: hxju@nju.edu.cn

Authors

Liu Qu − *Collaborative Innovation Center for Green Chemical Manufacturing and Accurate Detection, Key Laboratory of Interfacial Reaction & Sensing Analysis in Universities of Shandong, School of Chemistry and Chemical Engineering, University of Jinan, Jinan 250022, Shandong, China*

Lei Yang − *Collaborative Innovation Center for Green Chemical Manufacturing and Accurate Detection, Key Laboratory of Interfacial Reaction & Sensing Analysis in Universities of Shandong, School of Chemistry and Chemical Engineering, University of Jinan, Jinan 250022, Shandong, China*; orcid.org/0000-0003-2153-3570

Yueyuan Li − *School of Chemistry and Chemical Engineering, Shandong University of Technology, Zibo 255049, China*

Xiang Ren − *Collaborative Innovation Center for Green Chemical Manufacturing and Accurate Detection, Key Laboratory of Interfacial Reaction & Sensing Analysis in Universities of Shandong, School of Chemistry and Chemical Engineering, University of Jinan, Jinan 250022, Shandong, China*; orcid.org/0000-0002-4321-4282

Huan Wang − *Collaborative Innovation Center for Green Chemical Manufacturing and Accurate Detection, Key Laboratory of Interfacial Reaction & Sensing Analysis in Universities of Shandong, School of Chemistry and Chemical Engineering, University of Jinan, Jinan 250022, Shandong, China*

Dawei Fan − *Collaborative Innovation Center for Green Chemical Manufacturing and Accurate Detection, Key Laboratory of Interfacial Reaction & Sensing Analysis in Universities of Shandong, School of Chemistry and Chemical Engineering, University of Jinan, Jinan 250022, Shandong, China*

Complete contact information is available at: https://pubs.acs.org/10.1021/acsami.0c20049

Notes

The authors declare no competing financial interest.

■ ACKNOWLEDGMENTS

This study was supported by the National Key Scientific Instrument and Equipment Development Project of China (No. 21627809), the National Natural Science Foundation of China (No. 21777056), the Special Foundation for Taishan Scholar Professorship of Shandong Province, Jinan Scientific Research Leader Workshop Project (2018GXRC024 and 2018GXRC021), and the Innovation Team Project of Colleges and Universities in Jinan (No. 2019GXRC027).

■ REFERENCES

(1) Bansal, P.; Osman, D.; Gan, G. N.; Simon, G. R.; Boumber, Y. Recent Advances in Immunotherapy in Metastatic NSCLC. *Front. Oncol.* **2016**, *6*, 239.

(2) Williamson, J. Atezolizumab in Patients with Metastatic NSCLC. *Lancet Resp. Med.* **2018**, *6*, 584.

(3) Guowei, H.; Yuan, L.; Ma, L.; Zhongyang, L.; Zhixing, S.; Lin, L.; Minqi, L. The Diagnostic Efficacy of CYFRA21-1 on Intrahepatic Cholangiocarcinoma: A Meta-Analysis. *Clin. Res. Hepatol. Gastroenterol.* **2019**, *43*, 266−272.

(4) Jassem, J. Erlotinib as Adjuvant Therapy in EGFR-Mutant NSCLC. *Lancet Respir. Med.* **2018**, *6*, 808−810.

(5) Yang, L.; Jia, Y.; Wu, D.; Zhang, Y.; Ju, H.; Du, Y.; Ma, H.; Wei, Q. Synthesis and Application of CeO_2/SnS_2 Heterostructures as a Highly Efficient Coreaction Accelerator in the Luminol-Dissolved O_2 System for Ultrasensitive Biomarkers Immunoassay. *Anal. Chem.* **2019**, *91*, 14066−14073.

(6) Qian, Y.; Feng, J.; Xu, R.; Fan, D.; Du, Y.; Ren, X.; Wei, Q.; Ju, H. Zinc and Molybdenum Co-Doped $BiVO_4$ Nanoarray for Photoelectrochemical Diethylstilbestrol Analysis Based on the Dual-

Competitive System of Manganese Hexacyanoferrate Hydrate Nanocubes. *ACS Appl. Mater. Interfaces* **2020**, *12*, 16662−16669.
(7) Li, X.; Du, Y.; Wang, H.; Ma, H.; Wu, D.; Ren, X.; Wei, Q.; Xu, J.-J. Self-Supply of H_2O_2 and O_2 by Hydrolyzing CaO_2 to Enhance the Electrochemiluminescence of Luminol Based on a Closed Bipolar Electrode. *Anal. Chem.* **2020**, *92*, 12693−12699.
(8) Li, Y.; Liu, L.; Wang, Y.; Ren, R.; Fan, D.; Wu, D.; Du, Y.; Xu, K.; Ren, X.; Wei, Q.; Ju, H. Enzyme-Free Colorimetric Immunoassay for Procalcitonin Based on $MgFe_2O_4$ Sacrificial Probe with the Prussian Blue Production. *Sens. Actuators, B* **2020**, *316*, No. 128163.
(9) Li, Y.; Liu, L.; Liu, X.; Ren, Y.; Xu, K.; Zhang, N.; Sun, X.; Yang, X.; Ren, X.; Wei, Q. A Dual-Mode PCT Electrochemical Immunosensor with $CuCo_2S_4$ Bimetallic Sulfides as Enhancer. *Biosens. Bioelectron.* **2020**, *163*, No. 112280.
(10) Qu, L.; Yang, L.; Ren, Y.; Ren, X.; Fan, D.; Xu, K.; Wang, H.; Li, Y.; Ju, H.; Wei, Q. A Signal-Off Electrochemical Sensing Platform Based on Fe_3S_4-Pd and Pineal Mesoporous Bioactive Glass for Procalcitonin Detection. *Sens. Actuators, B* **2020**, *320*, No. 128324.
(11) Shao, K.; Wang, B.; Nie, A.; Ye, S.; Ma, J.; Li, Z.; Lv, Z.; Han, H. Target-Triggered Signal-On Ratiometric Electrochemiluminescence Sensing of PSA Based on MOF/Au/G-Quadruplex. *Biosens. Bioelectron.* **2018**, *118*, 160−166.
(12) Fan, Z.; Lin, Z.; Wang, Z.; Wang, J.; Xie, M.; Zhao, J.; Zhang, K.; Huang, W. Dual-Wavelength Electrochemiluminescence Ratiometric Biosensor for NF-κB p50 Detection with Dimethylthiodiaminoterephthalate Fluorophore and Self-Assembled DNA Tetrahedron Nanostructures Probe. *ACS Appl. Mater. Interfaces* **2020**, *12*, 11409−11418.
(13) Chen, Y.; Wang, X.-Y.; Wang, A.-J.; Mei, L.-P.; Yuan, P.-X.; Luo, X.; Feng, J.-J. Ultrasensitive Ratiometric Electrochemical Immunoassay of N-Terminal Pro-B-Type Natriuretic Peptide Based on Three-Dimensional PtCoNi Hollow Multi-Branches/Ferrocene-Grafted-Ionic Liquid and CoNC Nanosheets. *Sens. Actuators, B* **2021**, *326*, No. 128794.
(14) Hu, Y.; Yang, Z.; Lu, X.; Guo, J.; Cheng, R.; Zhu, L.; Wang, C.-F.; Chen, S. Facile Synthesis of Red Dual-Emissive Carbon Dots for Ratiometric Fluorescence Sensing and Cellular Imaging. *Nanoscale* **2020**, *12*, 5494−5500.
(15) Li, N.; Wang, Y.; Li, Y.; Cao, W.; Ma, H.; Wu, D.; Du, B.; Wei, Q. A Label-Free Electrochemical Immunosensor Based on Au@Pd/Ag Yolk-Bimetallic Shell Nanoparticles and Amination Graphene for Detection of Nuclear Matrix Protein 22. *Sens. Actuators, B* **2014**, *202*, 67−73.
(16) Guo, Y.; Wu, J.; Li, J.; Ju, H. A Plasmonic Colorimetric Strategy for Biosensing through Enzyme Guided Growth of Silver Nanoparticles on Gold Nanostars. *Biosens. Bioelectron.* **2016**, *78*, 267−273.
(17) Wang, Y.; Zhao, G.; Zhang, Y.; Pang, X.; Cao, W.; Du, B.; Wei, Q. Sandwich-Type Electrochemical Immunosensor for CEA Detection Based on Ag/MoS_2@Fe_3O_4 and an Analogous ELISA Method with Total Internal Reflection Microscopy. *Sens. Actuators, B* **2018**, *266*, 561−569.
(18) Xu, R.; Lu, P.; Wu, B.; Wang, X.; Pang, X.; Du, B.; Fan, D.; Wei, Q. Using SiO_2/PDA-Ag NPs to Dual-Inhibited Photoelectrochemical Activity of CeO_2-CdS Composites Fabricated a Novel Immunosensor for BNP Ultrasensitive Detection. *Sens. Actuators, B* **2018**, *274*, 349−355.
(19) Wang, C.; Zhang, N.; Wei, D.; Feng, R.; Fan, D.; Hu, L.; Wei, Q.; Ju, H. Double Electrochemiluminescence Quenching Effects of Fe_3O_4@PDA-Cu_xO towards Self-Enhanced $Ru(bpy)_3^{2+}$ Functionalized MOFs with Hollow Structure and Its Application to Procalcitonin Immunosensing. *Biosens. Bioelectron.* **2019**, *142*, No. 111521.
(20) Lee, H.; Dellatore, S. M.; Miller, W. M.; Messersmith, P. B. Mussel-Inspired Surface Chemistry for Multifunctional Coatings. *Science* **2007**, *318*, 426.
(21) Li, F.; Wang, Z.; Chen, W.; Zhang, S. A Simple Strategy for One-Step Construction of Bienzyme Biosensor by In-Situ Formation of Biocomposite Film through Electrodeposition. *Biosens. Bioelectron.* **2009**, *24*, 3030−3035.
(22) Cui, K.; Yan, B.; Xie, Y.; Qian, H.; Wang, X.; Huang, Q.; He, Y.; Jin, S.; Zeng, H. Regenerable Urchin-Like Fe_3O_4@PDA-Ag Hollow Microspheres as Catalyst and Adsorbent for Enhanced Removal of Organic Dyes. *J. Hazard. Mater.* **2018**, *350*, 66−75.
(23) Pal, T.; Sau, T. K.; Jana, N. R. Reversible Formation and Dissolution of Silver Nanoparticles in Aqueous Surfactant Media. *Langmuir* **1997**, *13*, 1481−1485.
(24) Miao, T.; Zheng, J.; Wang, J.; Xu, J.; Alharbi, N. S.; Zhang, M. Facile Synthesis of Metal Nanoparticles Decorated Magnetic Hierarchical Carbon Microtubes with Polydopamine-Derived Carbon Layer for Catalytic Applications. *Dalton Trans.* **2018**, *47*, 16578−16586.
(25) Corma, A. From Microporous to Mesoporous Molecular Sieve Materials and Their Use in Catalysis. *Chem. Rev.* **1997**, *97*, 2373−2420.
(26) Zhao, D.; Feng, J.; Huo, Q.; Melosh, N.; Fredrickson, G.; Chmelka, B. F.; Stucky, G. Triblock Copolymer Syntheses of Mesoporous Silica with Periodic 50 to 300 Å Pores. *Science* **1998**, *279*, 549−552.
(27) Korytkova, E. N.; Pivovarova, L. N.; Drozdova, I. A.; Gusarov, V. V. Synthesis of Nanotubular Nickel Hydrosilicates and Nickel-Magnesium Hydrosilicates under Hydrothermal Conditions. *Glass Phys. Chem.* **2005**, *31*, 797−802.
(28) Korytkova, E. N.; Maslov, A. V.; Pivovarova, L. N.; Polegotchenkova, Y. V.; Povinich, V. F.; Gusarov, V. V. Synthesis of Nanotubular $Mg_3Si_2O_5(OH)_4$-$Ni_3Si_2O_5(OH)_4$ Silicates at Elevated Temperatures and Pressures. *Inorg. Mater.* **2005**, *41*, 743−749.
(29) Stafiej, A.; Pyrzynska, K. Adsorption of Heavy Metal Ions with Carbon Nanotubes. *Sep. Purif. Technol.* **2007**, *58*, 49−52.
(30) Zhao, W. W.; Xu, J. J.; Chen, H. Y. Photoelectrochemical Immunoassays. *Anal. Chem.* **2018**, *90*, 615−627.
(31) Zheng, J.; Zhang, M.; Guo, X.; Wang, J.; Xu, J. Boronic Acid Functionalized Magnetic Composites with Sandwich-Like Nanostructures as a Novel Matrix for PDGF Detection. *Sens. Actuators, B* **2017**, *250*, 8−16.
(32) Tang, J.; Gao, K.; Ou, Q.; Fu, X.; Man, S.-Q.; Guo, J.; Liu, Y. Calculation Extinction Cross Sections and Molar Attenuation Coefficient of Small Gold Nanoparticles and Experimental Observation of Their UV-Vis Spectral Properties. *Spectrochim. Acta, Part A* **2018**, *191*, 513−520.
(33) Du, Y.; Xue, J.; Sun, X.; Wu, D.; Liu, X.; Ju, H.; Yang, L.; Wei, Q. Oxygen Vacancy-Enhanced Electrochemiluminescence Sensing Strategy Using Luminol Thermally Encapsulated in Apoferritin as a Transducer for Biomarker Immunoassay. *Anal. Chem.* **2020**, *92*, 8472−8479.

https://dx.doi.org/10.1021/acsami.0c20049
ACS Appl. Mater. Interfaces 2021, 13, 5795−5802